High-Order Curvilinear Finite Elements for Axisymmetric Lagrangian Hydrodynamics

V. Dobrev, T. Kolev, R. Rieben

December 21, 2011

High-Order Curvilinear Finite Elements for Axisymmetric Lagrangian Hydrodynamics☆

Veselin A. Dobrev[a], Truman E. Ellis[b], Tzanio V. Kolev[a], Robert N. Rieben[c]

[a]*Center for Applied Scientific Computing, Lawrence Livermore National Laboratory*
[b]*Institute for Computational Engineering and Sciences, University of Texas at Austin*
[c]*Weapons and Complex Integration, B-Division, Lawrence Livermore National Laboratory*

Abstract

In this paper we present an extension of our general high-order curvilinear finite element approach for solving the Euler equations in a Lagrangian frame [1] to the case of axisymmetric problems. The numerical approximation of these equations is important in a number of applications of compressible shock hydrodynamics and the reduction of 3D problems with axial symmetry to 2D computations provides a significant computational advantage. Unlike traditional staggered-grid hydrodynamics (SGH) methods which use the so-called "area-weighting" scheme, we formulate our semi-discrete axisymmetric conservation laws directly in 3D and reduce them to a 2D variational form in a meridian cut of the original domain. This is a natural extension of the high-order curvilinear finite element framework we have developed for 2D and 3D problems in Cartesian geometry, leading to a rescaled momentum conservation equation which includes new radial terms in the pressure gradient and artificial viscosity forces. We show that this approach exactly conserves energy and we demonstrate via computational examples that it also excels at preserving symmetry in problems with symmetric initial conditions. We also demonstrate that our computational method does not produce spurious symmetry breaking near the axis of rotation, as is the case with many area-wighted approaches.

Keywords: Axisymmetric problems, Lagrangian hydrodynamics, High-order finite element methods

1. Introduction and Motivation

The Euler equations of compressible hydrodynamics describe complex, multi-material, high speed flow and shock wave propagation over general 2D and 3D computational domains. We are interested in Lagrangian numerical methods for these problems, where the equations are discretized and solved on a generally unstructured computational mesh that moves with the fluid velocity. Specifically, the goal of Lagrangian hydrodynamics is to solve the following system of conservation laws:

$$\text{Momentum Conservation:} \quad \rho \frac{dv}{dt} = \nabla \cdot \sigma, \quad (1)$$

$$\text{Mass Conservation:} \quad \frac{1}{\rho}\frac{d\rho}{dt} = -\nabla \cdot v, \quad (2)$$

$$\text{Energy Conservation:} \quad \rho \frac{de}{dt} = \sigma : \nabla v, \quad (3)$$

$$\text{Equation of Motion:} \quad \frac{dx}{dt} = v, \quad (4)$$

$$\text{Equation of State:} \quad \sigma = -EOS(\rho, e)I, \quad (5)$$

which involves the material derivative $\frac{d}{dt}$, the kinematic variables for the fluid velocity v and position x, and the

thermodynamic variables for the density ρ, pressure p and internal energy e of the fluid [2, 3]. The equation of state, EOS, is a constitutive relation which in the simplest case of a polytropic ideal gas with a constant adiabatic index $\gamma > 1$ has the form $p = (\gamma - 1)\rho e$. Our formulation uses a general stress tensor σ in order to accommodate the inclusion of anisotropic tensor artificial viscosity stresses (see Section 3.2) as well as more complex material constitutive relations. We also focus on purely Lagrangian methods, and do not consider the other components of a full Arbitrary Lagrangian-Eulerian (ALE) framework in this paper.

Three dimensional simulations of Lagrangian shock hydrodynamics are of great practical importance [3, 4, 5], but are also substantially more expensive than 2D calculations. Therefore, for problems with axial symmetry, the reduction of (1)–(5) to computations in a 2D meridian cut provides a significant computational advantage. In previous articles [6, 1], we developed a general framework for high-order Lagrangian discretization of the Euler equations using curvilinear finite elements. In this paper, we present the extension of this framework to axisymmetric problems and demonstrate its ability to both conserve energy exactly and maintain symmetry. The realization of both these goals concurrently has proven challenging for many axisymmetric discretization schemes.

Traditional staggered-grid hydrodynamics (SGH) Lagrangian methods for axisymmetric problems have used

the "area-weighted" method where the momentum equation is solved in 2D planar coordinates using the "area masses" at nodes while the internal energy equation is solved over the real volumes [7, 8]. This approach does not conserve total energy and can often lead to incorrect shock speeds, or cause spurious symmetry breaking in the internal energy field near the axis of rotation, leading to non-physical results as illustrated in Figure 1 and Figure 2. Preservation of physical symmetries is critical for inertial confinement fusion (ICF) simulations as uncertainties in whether non-symmetric results are due to numerical errors or physical processes can limit predictive capability. New SGH approaches have been proposed to address this deficiency [9, 10, 11, 12], which have led to significant improvements in energy and symmetry preservation. Other successful methods in this area include the special finite elements proposed in [13, 14] and the recent cell-centered hydro approach of [15]

Figure 2: Example of numerical symmetry breaking in an axisymmetric multi-material inertial confinement fusion (ICF) simulation. This is an ALE calculation where different colors are used to identify the different materials. The jet at the axis of rotation is spurious and does not disappear under mesh refinement.
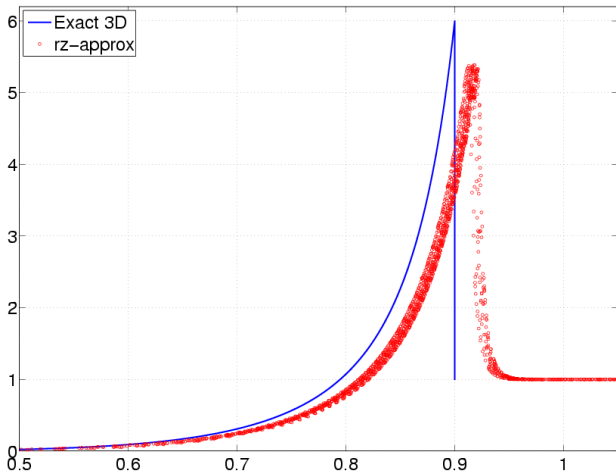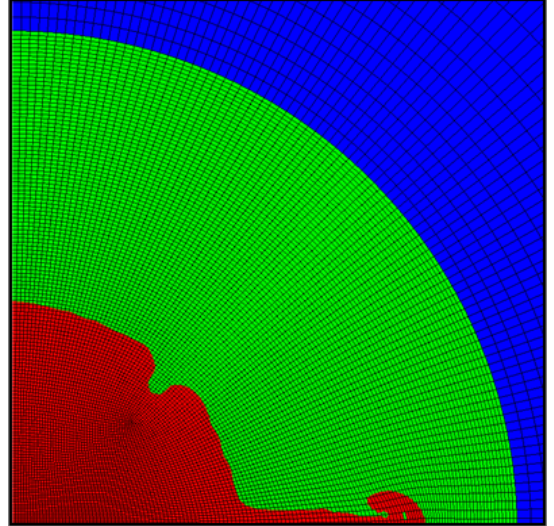

Figure 1: Scatter plot of the density from an SGH spherical Sedov blast wave in axisymmetric mode [16]. The exact solution corresponds to the blue line. While the "area-weighted" approach preserves the symmetry of accelerations, the corresponding energy update is not conservative. In this calculation this results in a 6% spurious gain in energy leading to incorrect shock speed and location. These do not improve under mesh refinement.

In contrast to the above schemes, our finite element numerical method is derived by a faithful reduction of the 3D axisymmetric problem to a 2D variational form in a meridian cut of the domain, which conserves total energy exactly by construction. Unlike the area-weighted scheme, this leads to a rescaled momentum conservation equation, which also includes new terms in the pressure gradient and artificial viscosity forces. As in Cartesian coordinates, the high-order finite element approach uses high-order basis function expansions obtained via a high-order mapping from a standard reference element. This enables the use of curvilinear zone geometry and higher order approximations for the fields within a zone.

The remainder of the paper is organized as follows. In Section 2 we introduce notation and recall some basic facts

about axisymmetric scalar, vector and tensor fields. These are used in Section 3, where we describe the derivation of our axisymmetric semi-discrete finite element method, followed by discussion of the artificial viscosity, the fully-discrete algorithm and the relation to some classical SGH methods. In Section 4, we present an extensive set of numerical results that demonstrate the robustness of our algorithm with respect to symmetry and energy conservation on a range of challenging axisymmetric problems. Finally, we summarize our experience and draw some conclusions in Section 5.

2. Axisymmetric Scalar, Vector and Tensor Fields

In this section we recall some basic facts about axisymmetric fields that will be used in the development of our finite element discretization method in the following section.

We assume that at any given time, the domain Ω occupied by the fluid is a body of revolution, as illustrated in Figure 3. In cylindrical coordinates (r, θ, z), Ω can be obtained from a "meridian cut" Γ in the r-z plane by a rotation around the axis $r = 0$:

$$\Omega = \{(r, \theta, z) \,:\, (r, z) \in \Gamma\}.$$

A scalar function f, defined on the axisymmetric domain Ω, is itself called axisymmetric if it is independent of θ, i.e. $f(r, \theta, z) = f(r, z)$, so f is uniquely determined by its values in Γ. If f is given in Cartesian coordinates, it is axisymmetric if and only if

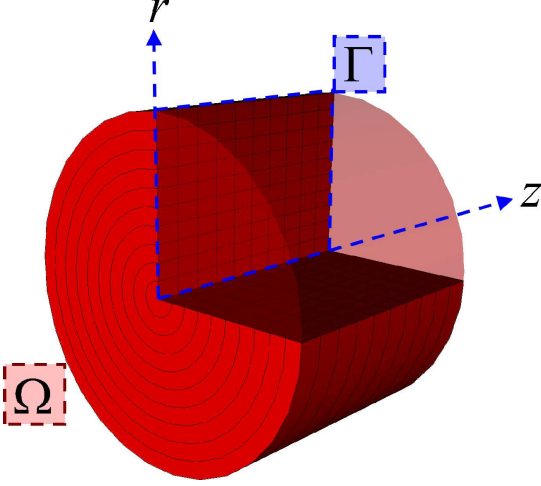$$\frac{\partial}{\partial \theta} f(r \cos \theta, r \sin \theta, z) = 0 \,,$$

Figure 3: Schematic depiction of the reduction of a 3D axisymmetric problem to a 2D "meridian cut" in the r-z plane.

i.e. if f is only spatially varying in the r-z plane

A key property of axisymmetric functions is that their integrals over Ω can be reduced to integrals over Γ:

$$\int_\Omega f(r,\theta,z) = 2\pi \int_\Gamma r f(r,z) \,. \tag{6}$$

The local cylindrical coordinate system vectors at a point (r,θ,z) are given by

$$\vec{e}_r = (\cos\theta, \sin\theta, 0)\,,\ \vec{e}_\theta = (-\sin\theta, \cos\theta, 0)\,,\ \vec{e}_z = (0,0,1)\,.$$

A vector field v, defined on the axisymmetric domain Ω, is called axisymmetric if

$$v = v_r(r,z)\vec{e}_r + v_\theta(r,z)\vec{e}_\theta + v_z(r,z)\vec{e}_z \,,$$

i.e. if v remains invariant under arbitrary rotation around the axis $r = 0$. In our applications, the above $v_\theta(r,z)$ component decouples from the other two, so without a loss of generality, we will further assume that $v_\theta(r,z) = 0$, i.e. axisymmetric vector fields do not have components in the normal direction of the meridian cut.

The gradient operator in cylindrical coordinates is given by

$$\nabla_{rz} f = \frac{\partial f}{\partial r}\vec{e}_r + \frac{1}{r}\frac{\partial f}{\partial \theta}\vec{e}_\theta + \frac{\partial f}{\partial z}\vec{e}_z \,. \tag{7}$$

Therefore, $\nabla_{rz} f$ is axisymmetric if and only if f is. In this case, the formula simplifies to

$$\nabla_{rz} f = \frac{\partial f}{\partial r}\vec{e}_r + \frac{\partial f}{\partial z}\vec{e}_z \,,$$

which is just the regular 2D gradient in Γ. Note that this property is one of the motivating factors for using area-weighting schemes, as it implies that gradient operators are unchanged in axisymmetric coordinates.

The divergence in cylindrical coordinates is more complicated:

$$\nabla_{rz} \cdot v = \frac{\partial v_r}{\partial r} + \frac{1}{r}\frac{\partial v_\theta}{\partial \theta} + \frac{\partial v_z}{\partial z} + \frac{v_r}{r} \,, \tag{8}$$

but $\nabla_{rz}\cdot v$ is still axisymmetric, provided that v is. In this case, the formula simplifies to

$$\nabla_{rz} \cdot v = \frac{\partial v_r}{\partial r} + \frac{\partial v_z}{\partial z} + \frac{v_r}{r} \,,$$

which has an extra term compared to the regular 2D divergence in Γ.

The gradient of the axisymmetric vector function $v = v_r(r,z)\vec{e}_r + v_z(r,z)\vec{e}_z$ can be derived using (7) and the fact that $\frac{\partial \vec{e}_r}{\partial \theta} = e_\theta$. Specifically,

$$\begin{aligned}
\nabla_{rz} v &= \frac{\partial v}{\partial r}\otimes\vec{e}_r + \frac{1}{r}\frac{\partial v}{\partial \theta}\otimes\vec{e}_\theta + \frac{\partial v}{\partial z}\otimes\vec{e}_z \\
&= \frac{\partial v_r}{\partial r}\vec{e}_r\otimes\vec{e}_r + \frac{\partial v_z}{\partial r}\vec{e}_z\otimes\vec{e}_r + \frac{v_r}{r}\vec{e}_\theta\otimes\vec{e}_\theta + \\
&\quad \frac{\partial v_r}{\partial z}\vec{e}_r\otimes\vec{e}_z + \frac{\partial v_z}{\partial z}\vec{e}_z\otimes\vec{e}_z \,,
\end{aligned}$$

so the matrix form of the gradient in the $z-r-\theta$ ordering is

$$\nabla_{rz} v = \begin{pmatrix} \frac{\partial v_z}{\partial z} & \frac{\partial v_z}{\partial r} & 0 \\ \frac{\partial v_r}{\partial z} & \frac{\partial v_r}{\partial r} & 0 \\ 0 & 0 & \frac{v_r}{r} \end{pmatrix} = \begin{pmatrix} \nabla_{2d} v & 0 \\ 0 & \frac{v_r}{r} \end{pmatrix} \,. \tag{9}$$

In particular, for the contraction of axisymmetric vector fields we have

$$\nabla_{rz} v : \nabla_{rz} w = \nabla_{2d} v : \nabla_{2d} w + \frac{v_r w_r}{r^2} \,,$$

which also implies the formula for the divergence in cylindrical coordinates:

$$\nabla_{rz} \cdot v = \nabla_{rz} v : I = \frac{\partial v_z}{\partial z} + \frac{\partial v_r}{\partial r} + \frac{v_r}{r} \,.$$

3. Finite Element Discretization

In this section we derive and discuss a finite element-based numerical approximation scheme for the Euler equations (1)–(5) in axisymmetric form. The presentation follows the finite element form of the general semi-discrete Lagrangian discretization method from [1], to which we refer for additional details.

3.1. Semi-Discrete Formulation

We first discuss the semi-discrete axisymmetric method, which is concerned only with the spatial approximation of the continuum equations. The fully-discrete methods that incorporate time discretization will be presented in Section 3.3.

Let $\Omega(t)$ be the continuous 3D axisymmetric medium (fluid or elastic body) which is deforming in time according to (1)–(5) starting from an initial configuration at time $t = t_0$. Let $\Gamma(t)$ be the corresponding meridian cut, as discussed in Section 2. Following [1], we introduce a 2D finite element mesh on $\widetilde{\Gamma} \equiv \Gamma(t_0)$ with zones (or elements) $\{\Gamma_z(t_0)\}$. This also induces a decomposition of $\widetilde{\Omega} \equiv \Omega(t_0)$ into "donut"-like zones $\{\Omega_z(t_0)\}$ obtained by revolution of

3

the 2D mesh elements around the axis $r = 0$ in cylindrical coordinates:

$$\Omega_z(t_0) = \{(r, \theta, z) \,:\, (r, z) \in \Gamma_z(t_0)\}. \quad (10)$$

A main feature of our approach is that the finite element mesh is described through the locations of high-order particles (or control points) that are tracked by the semi-discrete algorithm. This results in curvilinear zones that can better represent the naturally developing curvature in the flow. Specifically, the current position at time t, $x \in \Gamma(t)$, corresponding to a particle at an initial position $\tilde{x} \in \widetilde{\Gamma}$ is discretized using the expansion

$$x(\tilde{x}, t) = \sum_{i=1}^{N_v} \mathbf{x}_i(t) w_i(\tilde{x}) = \mathbf{x}(t)^{\mathrm{T}} \mathbf{w}(\tilde{x}), \quad (11)$$

where $\mathbf{x}(t)$ is an unknown time-dependent vector of coefficients in the kinematic basis $\{w_i\}_{i=1}^{N_v}$, and $\mathbf{w}$ is a column vector of all the basis functions $\{w_i\}$. The kinematic basis functions are defined through Cartesian products of nodal finite element basis functions $\{\hat{\eta}_i\}_{i=1}^{N_v}$ defined on a standard reference zone $\widehat{\Gamma}_z$, which is the unit square in all cases considered in this paper. The curvilinear zones at time t are then reconstructed as

$$\Gamma_z(t) = \{x = \Phi_z(\hat{x}, t) : \hat{x} \in \widehat{\Gamma}_z\}, \quad (12)$$

where Φ_z is the parametric mapping from the reference element

$$\Phi_z(\hat{x}, t) = \sum_{i=1}^{N_v} x_{z,i}(t)\, \hat{\eta}_i(\hat{x}). \quad (13)$$

We denote the Jacobian of this mapping by $\mathbf{J}_z = \nabla_{\hat{x}} \Phi_z$.

Note that the same nodal basis is used for discretization of both the position and the velocity, so each component of a $w_i|_{\Gamma_z}$ corresponds to $\hat{\eta}_p \circ \Phi_z^{-1}$ for some index p (the index of the particle i on the reference element). The discrete velocity field corresponding to the motion (11) is given by

$$v(\tilde{x}, t) = \sum_i \frac{d\mathbf{x}_i}{dt}(t) w_i(\tilde{x}) = \mathbf{v}(t)^{\mathrm{T}} \mathbf{w}(\tilde{x}), \quad \text{i.e.} \quad \mathbf{v} = \frac{d\mathbf{x}}{dt}$$

in agreement with (4).

We next discuss the reduction of the mass conservation law, which is fundamental in the Lagrangian framework. We start from the following equivalent form of (2): let $\Omega'(t)$ be the revolution of an arbitrary set $\Gamma'(t) \subset \Gamma(t)$, then we mass conservation postulates that

$$\int_{\Omega'(t)} \rho(t) = \int_{\Omega'(t_0)} \rho(t_0),$$

i.e. the total mass in any axisymmetric volume $\Omega'(t)$ at time t equals the initial mass at time t_0. Due to (6), this is equivalent to

$$2\pi \int_{\Gamma'(t)} r\rho(t) = 2\pi \int_{\Gamma'(t_0)} r\rho(t_0).$$

Since $\Gamma'(t)$ is arbitrary, we can reduce this further using a change of variables to the reference element to obtain:

$$r(t)\rho(t)|\mathbf{J}_z(t)| = r(t_0)\rho(t_0)|\mathbf{J}_z(t_0)|. \quad (14)$$

We refer to the above semi-discrete principle as *strong mass conservation*, and we note that the only difference between this axisymmetric version and the Cartesian version from (4.8) in [1] is the extra r term on both sides of (14). Strong mass conservation allows us to express the density at time t as a (non-polynomial) function of the original density, effectively eliminating ρ from the semi-discrete algorithm, and can be vied as a high order generalization of zonal mass conservation. Though (14) is not well-defined on the axis of rotation, we will only apply it at points where $r \neq 0$.

We now focus on the derivation of the axisymmetric form of the momentum conservation equation. Multiplying (1) by a revolved test function w_j and integrating by parts, we get the weak variational formulation

$$\int_{\Omega(t)} \rho \frac{dv}{dt} \cdot w_j = -\int_{\Omega(t)} \sigma : \nabla w_j + \int_{\partial\Omega(t)} n \cdot \sigma \cdot w_j, \quad (15)$$

where n is the outward pointing unit normal vector of the surface $\partial\Omega(t)$. Assuming the boundary integral term vanishes and applying (6) we obtain

$$2\pi \int_{\Gamma(t)} r\rho \frac{dv}{dt} \cdot w_j = -2\pi \int_{\Gamma(t)} r\sigma_{rz} : \nabla_{rz} w_j. \quad (16)$$

Using (9) and contraction of axisymmetric tensors, we can write (16) in the form

$$\int_{\Gamma(t)} r\rho \frac{dv}{dt} \cdot w_j = -\int_{\Gamma(t)} r\left(\sigma_{2d} : \nabla_{2d} w_j\right) - p(w_j)_r + \sigma_{rr}(w_j)_r,$$

where σ_{2d} and ∇_{2d} are just the regular 2D stress and gradient tensors in Γ. This can be viewed as a perturbation of the Cartesian case, where the weak variational formulation reads

$$\int_{\Gamma(t)} \rho \frac{dv}{dt} \cdot w_j = -\int_{\Gamma(t)} \sigma_{2d} : \nabla_{2d} w_j.$$

We emphasize that even though the two versions are similar, they are not the same due to the r weighing of the integrals and the extra pressure and stress-related terms on the right-hand side of the axisymmetric case. This is in contrast to the "area-weighting" scheme which essentially uses the Cartesian form in axisymmetric computations. While our approach is more faithful to the original 3D equations on Ω, we do not automatically inherit the symmetry-preservation properties of the Cartesian form. Nevertheless, we do observe good symmetry preservation in practice as illustrated in Section 4.

Let $\mathbf{M}_{\mathcal{V}}$ be the *axisymmetric kinematic mass matrix* (we skip the 2π factor)

$$\mathbf{M}_{\mathcal{V}} = \int_{\Gamma(t)} r\rho \mathbf{w}\mathbf{w}^{\mathrm{T}}, \quad (17)$$

4

where we have defined the basis $\mathbf{w}(t)$ by moving $\mathbf{w}(t_0)$ according to the Lagrangian motion (11). This means that $\frac{d\mathbf{w}}{dt} = 0$, which together with (14) implies

$$\frac{d\mathbf{M}_{\mathcal{V}}}{dt} = 0,$$

i.e., the kinematic mass matrix is independent of time. This is an important feature of our approach.

With this notation, we can write our semi-discrete momentum conservation briefly as

$$\mathbf{M}_{\mathcal{V}} \frac{d\mathbf{v}}{dt} = -\int_{\Gamma(t)} r\sigma_{rz} : \nabla_{rz}\mathbf{w}. \qquad (18)$$

To discretize the energy conservation law, we introduce a thermodynamic approximation space with basis $\{\phi_i\}_{j=1}^{N_{\mathcal{E}}}$ which is analogous to the kinematic basis, except that it is discontinuous (we make this choice due to the local nature of the equation of state). The internal energy is then approximated as

$$e(\tilde{x}, t) = \sum_j \mathbf{e}_j(t)\phi_j(\tilde{x}) = \mathbf{e}(t)^{\mathrm{T}}\boldsymbol{\phi}(\tilde{x}),$$

where $\mathbf{e}(t)$ is an unknown time-dependent vector of size $N_{\mathcal{E}}$ and $\boldsymbol{\phi}(\tilde{x})$ is a column vector of all the basis functions $\{\phi_j\}_{j=1}^{N_{\mathcal{E}}}$.

The weak variational formulation of the energy conservation equation (3) is obtained by multiplying it by ϕ_i and integrating over the domain $\Omega(t)$:

$$\int_{\Omega(t)} \left(\rho \frac{de}{dt} \right) \phi_i = \int_{\Omega(t)} (\sigma : \nabla v)\, \phi_i. \qquad (19)$$

Using (6), this reads

$$2\pi \int_{\Gamma(t)} r \left(\rho \frac{de}{dt} \right) \phi_i = 2\pi \int_{\Gamma(t)} r(\sigma_{rz} : \nabla_{rz}v)\, \phi_i,$$

which can be written briefly as

$$\mathbf{M}_{\mathcal{E}} \frac{d\mathbf{e}}{dt} = \int_{\Gamma(t)} r(\sigma_{rz} : \nabla_{rz}v)\, \boldsymbol{\phi}, \qquad (20)$$

where $\mathbf{M}_{\mathcal{E}}$ is the *axisymmetric thermodynamic mass matrix*

$$\mathbf{M}_{\mathcal{E}} \equiv \int_{\Gamma(t)} r\rho\boldsymbol{\phi}\boldsymbol{\phi}^{\mathrm{T}}. \qquad (21)$$

Similarly to $\mathbf{M}_{\mathcal{V}}$, this matrix is independent of time.

We finally introduce the so-called *axisymmetric force matrix* that connects the kinematic and thermodynamic spaces:

$$\mathbf{F}_{ij} = \int_{\Gamma(t)} r\left(\sigma_{rz} : \nabla_{rz}w_i \right) \phi_j. \qquad (22)$$

This allows us to summarize our axisymmetric semi-discrete Lagrangian conservation laws in the following simple form:

Momentum Conservation: $\quad \mathbf{M}_{\mathcal{V}} \dfrac{d\mathbf{v}}{dt} = -\mathbf{F} \cdot \mathbf{1},$ (23)

Energy Conservation: $\quad \mathbf{M}_{\mathcal{E}} \dfrac{d\mathbf{e}}{dt} = \mathbf{F}^{\mathrm{T}} \cdot \mathbf{v},$ (24)

Equation of Motion: $\quad \dfrac{d\mathbf{x}}{dt} = \mathbf{v}.$ (25)

Here $\mathbf{1}$ is a vector representing the constant one in the thermodynamic basis $\{\phi_i\}$.

The above semi-discrete form is identical to the one from the 2D Cartesian case [1], with the only differences being the r-scaling in the integrals and the extra terms in the force matrix. In particular, the time independence of the mass matrices and the compatible right-hand sides of (24) and (25) imply that the above semi-discrete scheme will conserve total energy exactly on a semi-discrete level. The proof of this fact can be found in [1]; we present it below for completeness.

The change in the total energy

$$E(t) = \int_{\Omega(t)} \rho \frac{|v|^2}{2} + \rho\, e \qquad (26)$$

can be expressed in the semi-discrete settings using (6) as:

$$\frac{dE}{dt} = 2\pi \frac{d}{dt} \left(\frac{1}{2}\, \mathbf{v} \cdot \mathbf{M}_{\mathcal{V}} \cdot \mathbf{v} + \mathbf{1} \cdot \mathbf{M}_{\mathcal{E}} \cdot \mathbf{e} \right).$$

Using the fact that both the kinematic and thermodynamic mass matrices are symmetric and independent of time, as well as equations (23) and (24), we get

$$\frac{1}{2\pi} \frac{dE}{dt} = \mathbf{v} \cdot \mathbf{M}_{\mathcal{V}} \cdot \frac{d\mathbf{v}}{dt} + \mathbf{1} \cdot \mathbf{M}_{\mathcal{E}} \cdot \frac{d\mathbf{e}}{dt} = -\mathbf{v} \cdot \mathbf{F} \cdot \mathbf{1} + \mathbf{1} \cdot \mathbf{F}^{\mathrm{T}} \cdot \mathbf{v} = 0,$$

i.e. the total energy remains constant in time.

Remark 1. *As an alternative to the more explicit Γ-based perspective presented in this section, one can also consider the direct discretization of the 3D domain Ω using the rotated versions of the finite element mesh, cf. (10), as well as the kinematic and thermodynamic spaces. Though the resulting 3D approximation spaces $\mathcal{V}$ and $\mathcal{E}$ are not of finite element type, they are finite dimensional, so the abstract semi-discrete Lagrangian variational formulation from Section 3 in [1] still applies. In particular, we can conclude that the above semi-discrete equations (with integrals computed e.g. by reduction to the meridian cut) exactly satisfy the properties of mass, momentum and energy conservation as well as the geometric conservation law, based on Theorem 3.1 from [1].*

3.2. Axisymmetric Tensor Artificial Viscosity

In this section we briefly outline the modifications to the tensor artificial viscosity term from Section 6 in [1] which are necessary for the axisymmetric case. The changes are minor, so we simply outline them for the specific case of the artificial stress option 2,

$$\sigma_{a,2} = \mu\varepsilon(v). \qquad (27)$$

Similar considerations apply to the other viscosity types considered in [1].

First, we note that the symmetrized gradient of the velocity field,

$$\varepsilon(v) \equiv \frac{1}{2}(\nabla v + v\nabla),$$

has the following form in the axisymmetric case (using the $z - r - \theta$ ordering from Section 2)

$$\varepsilon(v) = \begin{pmatrix} \varepsilon_{2d}(v) & 0 \\ 0 & \frac{v_r}{r} \end{pmatrix}$$

where $\varepsilon_{2d}(v)$ is simply the symmetrized gradient in Γ. There is no problem with division by zero in the rr-component of the stress tensor, since when it is used in the force computations of (22), $\varepsilon(v)_{rr}$ generates the extra term $\frac{v_r}{r}(w_i)_r \phi_j$, which is zero on $r = 0$ due to the boundary conditions of symmetry in the kinematic space. Furthermore, $\sigma_{a,2}$ is only being evaluated at Gaussian quadrature points, which all have $r \neq 0$.

The coefficient μ in (27) is based on a "shock direction" vector s, which we assume to lie in the meridian cut plane Γ, i.e. we ignore the $\vec{e}_\theta$ eigenvector of $\varepsilon_{rz}(v)$ and compute s only from $\varepsilon_{2d}(v)$ (same as in 2D).

The overall form of the directional viscosity coefficient is

$$\mu_s = \tilde{\rho}\big[q_2 \psi_2 \ell_s^2 |\Delta_s v| + q_1 \psi_0 \psi_1 \ell_s c_s\big]$$

where we use the axisymmetric strong mass conservation to compute $\tilde{\rho}$:

$$\tilde{\rho} = \rho(t_0) \frac{r(t_0)|J_z(t_0)|}{r(t)|J_z(t)|}.$$

The measure of compression $|\Delta_s v|$ and the directional length scale ℓ_s are the same as in 2D because s lies in Γ. The only other difference is in the vorticity/compression measure, which incorporates the rz divergence of (8)

$$\psi_0 = \frac{|\nabla_{2d} \cdot v + v_r/r|}{\sqrt{\|\nabla_{2d} v\|^2 + |v_r/r|^2}}.$$

Again, division by zero on the axis $r = 0$ does not arise, since the Gaussian quadrature points in which ψ_0 is being evaluated are in the interior of the computational zones.

3.3. Fully-discrete Method

Let $\{t_n\}_{n=0}^{N_t}$ be different moments in time and denote $\Gamma^n \equiv \Gamma(t_n)$ and $\Omega^n \equiv \Omega(t_n)$. We use a superscript n to identify the quantities associated with t_n.

As in [1], let $Y = (\mathbf{v}; \mathbf{e}; \mathbf{x})$ be a vector of the hydrodynamic state variables. Our semi-discrete conservation equations then are:

$$\frac{\mathrm{d}Y}{\mathrm{d}t} = \mathcal{F}(Y, t),$$

where

$$\mathcal{F}(Y, t) = \begin{pmatrix} \mathcal{F}_v(\mathbf{v}, \mathbf{e}, \mathbf{x}) \\ \mathcal{F}_e(\mathbf{v}, \mathbf{e}, \mathbf{x}) \\ \mathcal{F}_x(\mathbf{v}, \mathbf{e}, \mathbf{x}) \end{pmatrix} = \begin{pmatrix} -\mathbf{M}_\mathcal{V}^{-1} \mathbf{F} \cdot \mathbf{1} \\ \mathbf{M}_\mathcal{E}^{-1} \mathbf{F}^{\mathrm{T}} \cdot \mathbf{v} \\ \mathbf{v} \end{pmatrix}$$

We can apply standard high-order time integration solvers to the above system of nonlinear ODEs, including variants of explicit Runge-Kutta methods, such as the RK2-Average scheme from Section 7.1 in [1]:

$$\mathbf{v}^{n+\frac{1}{2}} = \mathbf{v}^n - (\Delta t/2)\,\mathbf{M}_\mathcal{V}^{-1}\mathbf{F}^n \cdot \mathbf{1},$$
$$\mathbf{e}^{n+\frac{1}{2}} = \mathbf{e}^n + (\Delta t/2)\,\mathbf{M}_\mathcal{E}^{-1}(\mathbf{F}^n)^{\mathrm{T}} \cdot \mathbf{v}^{n+\frac{1}{2}},$$
$$\mathbf{x}^{n+\frac{1}{2}} = \mathbf{x}^n + (\Delta t/2)\,\mathbf{v}^{n+\frac{1}{2}},$$
$$\mathbf{v}^{n+1} = \mathbf{v}^n - \Delta t\,\mathbf{M}_\mathcal{V}^{-1}\mathbf{F}^{n+\frac{1}{2}} \cdot \mathbf{1},$$
$$\mathbf{e}^{n+1} = \mathbf{e}^n + \Delta t\,\mathbf{M}_\mathcal{E}^{-1}(\mathbf{F}^{n+\frac{1}{2}})^{\mathrm{T}} \cdot \bar{\mathbf{v}}^{n+\frac{1}{2}},$$
$$\mathbf{x}^{n+1} = \mathbf{x}^n + \Delta t\,\bar{\mathbf{v}}^{n+\frac{1}{2}},$$

where $\mathbf{F}^n = \mathbf{F}(Y^n)$ and $\bar{\mathbf{v}}^{n+\frac{1}{2}} = (\mathbf{v}^n + \mathbf{v}^{n+1})/2$. This choice has the attractive property that it conserves the discrete total energy exactly [1] and is the default time integrator in the numerical experiments in Section 4.

Our automatic time-step control for determining Δt is based on the density, sound speed, viscosity coefficient and minimal singular values of the Jacobian $\mathbf{J}_z$, which do not require any modifications in the axisymmetric case.

3.4. Relation to SGH Methods

In this section we describe several connections between our finite element framework and some classical discretization schemes under additional discretization assumptions.

As in Section 5.1 of [1], we first consider the evaluation of the kinematic mass matrix in the case of piecewise bilinear kinematic approximation and a single point quadrature rule with mass lumping. This produces a diagonal matrix, with "nodal masses"

$$m_n = \sum_{\Gamma_z \ni n} \frac{1}{4} r_z \rho_z |\Gamma_z|,$$

where $|\Gamma_z|$ is area of the zone, r_z and ρ_z denote the values of r and the density in the zone center, and the sum is taken over all zones containing a fixed node (vertex) n. We can write this as

$$m_n = \sum_{\Gamma_z \ni n} r_z m_z^{2d}, \quad \text{where} \quad m_z^{2d} = \frac{1}{4}\rho_z |\Gamma_z|,$$

which is an r-weighted version of the two-dimensional SGH nodal masses from [7].

Applying the same one point quadrature rule in the computation of the force representing the right-hand side of the momentum equation we get (analogously to [1])

$$f_n = \sum_{\Gamma_z \ni n} \mathbf{f}_z,$$

where the axisymmetric *corner force* vector $\mathbf{f}_z$ relates to the 2D HEMP corner forces $\mathbf{f}_z^{2d}$ of [7] as follows:

$$\mathbf{f}_z = r_z \mathbf{f}_z^{2d} + \frac{p_z |\Gamma_z|}{4} \begin{pmatrix} 0 \\ 1 \end{pmatrix}_{z-r},$$

i.e. $\mathbf{f}_z$ is an r-weighted version of $\mathbf{f}_z^{2d}$ plus an extra pressure term in its r component.

To summarize, under the specified simplifying assumptions, our axisymmetric momentum equation for the nodal accelerations a_n reads

$$\left(\sum_{\Gamma_z \ni n} r_z m_z^{2d}\right) a_n = \sum_{\Gamma_z \ni n} r_z \mathbf{f}_z^{2d} + \frac{p_z |\Gamma_z|}{4}\begin{pmatrix} 0 \\ 1 \end{pmatrix}. \quad (28)$$

which is similar to, but differs from the "area-weighted" (Cartesian) version

$$\left(\sum_{\Gamma_z \ni n} m_z^{2d}\right) a_n^{2d} = \sum_{\Omega_z \ni n} \mathbf{f}_z^{2d}.$$

We next discuss the discretization of the internal energy equation in the case of piece-wise constant thermodynamic basis. In the Wilkins approach, [7] the rz velocity divergence in the center of a zone is approximated through the rate of change of its revolved volume

$$\frac{1}{|\Omega_z(t)|}\frac{d|\Omega_z(t)|}{dt} = \nabla \cdot v. \quad (29)$$

This formula is related to the so-called geometric conservation law,

$$\frac{d|\Omega(t)|}{dt} = \int_{\Omega(t)} \nabla \cdot v, \quad (30)$$

but we remark that unlike the Cartesian case, (29) is only an approximation to, and not equivalent with (30).

In the general *compatible hydro* approach [17, 9, 18], the right-hand side of the energy equation is computed through the corner forces computed in the momentum equation:

$$m_z \frac{de_z}{dt} = -\mathbf{f}_z \cdot \mathbf{v}_z. \quad (31)$$

It is straightforward to check that we recover a formula of the above type under the simplifying assumptions, with

$$m_z = \rho_z |\Omega_z| \quad \text{and} \quad \mathbf{v}_z = \sum_{n \in \Gamma_z} v_n.$$

We comment that our simplified SGH-like scheme based on (28) and (31) inherits the exact total energy conservation property, in the sense that

$$\frac{d}{dt}\left(\sum_n m_n \frac{|v_n|^2}{2} + \sum_{\Gamma_z} m_z e_z\right) = 0.$$

Indeed, assuming constant nodal masses,

$$\frac{d}{dt}\sum_n m_n \frac{|v_n|^2}{2} = \sum_n m_n a_n \cdot v_n = \sum_n f_n \cdot v_n$$

but

$$\sum_n f_n \cdot v_n = \sum_{\Gamma_z} \mathbf{f}_z \cdot \sum_{n \in \Gamma_z} v_n = -\frac{d}{dt}\sum_{\Gamma_z} m_z e_z$$

which completes the proof.

4. Numerical Results

We now present a series of numerical results using the newly developed axisymmetric curvilinear finite element formulation. For all test cases considered, we solve the global linear system for momentum conservation using a diagonally scaled conjugate gradient algorithm to a residual tolerance of 10^{-8} and unless otherwise specified, we use an ideal gas equation of state with a constant adiabatic index $\gamma = 5/3$ and the type 2 tensor artificial viscosity described in [1] with linear and quadratic coefficients $q_1 = 1/2$ and $q_2 = 2$. Furthermore, in most of these examples we only consider the use of a Q_2-Q_1 method for the sake of brevity. The only exception is Section 4.4 where we consider a Q_4-Q_3 method to demonstrate that our axisymmetric formulation is valid for arbitrary order basis functions as described in [1]. The axisymmetric Q_2-Q_1 method consists of 9 kinematic degrees of freedom per zone and 4 discontinuous thermodynamic degrees of freedom per zone. The results in this section have been computed with our high-order finite element Lagrangian hydrocode BLAST [19], which is based on the parallel modular finite element methods library MFEM [20]. We also used the related OpenGL visualization tool GLVis [21] to plot the computed curvilinear meshes and high-order fields.

4.1. Cylindrical Saltzman Piston

In this test problem, a 1D piston shock wave is propagated over an initially distorted 2D mesh. The problem domain is a cylinder with $z \in [0,1]$ and $r \in [0, 0.1]$ with initial thermodynamic conditions $\rho = 1$, $p = 0$ and $e = 0$. The details of how the initial skewed mesh is constructed can be found in [22]. The velocity is initially zero everywhere except at the wall $x = 0$, where a constant velocity source of $v_x = 1.0$ is applied for all time. This problem tests the ability of our axisymmetric methods to maintain a 1D planar shock front on a mesh that is not aligned with the shock flow and provides and indication of the robustness of our method with respect to mesh imprinting. It is also a good test of possible symmetry breaking near the axis of rotation.

In Figure 4 we plot the density field and curvilinear mesh at snapshots in time corresponding to $t = 0.7, 0.8, 0.88, 0.92, 0.94, 0.96, 0.975, 0.985, 0.987, 0.99$ and 0.992. Note that the shock front has bounced from the boundary walls for a total of seven times. To our knowledge this is the latest time to which this problem has been shown to run in a purely Lagrangian manner. Note also that the shock front remains largely flat for all time and only at extremely late times do we begin to observe the minor effect of symmetry breaking near the axis of rotation.

4.2. Spherical Sedov Explosion

The Sedov problem consists of an ideal gas ($\gamma = 1.4$) with a delta function source of internal energy deposited at the origin such that the total energy $E_{tot} = 1$. The sudden release of the energy creates an expanding spherical shock
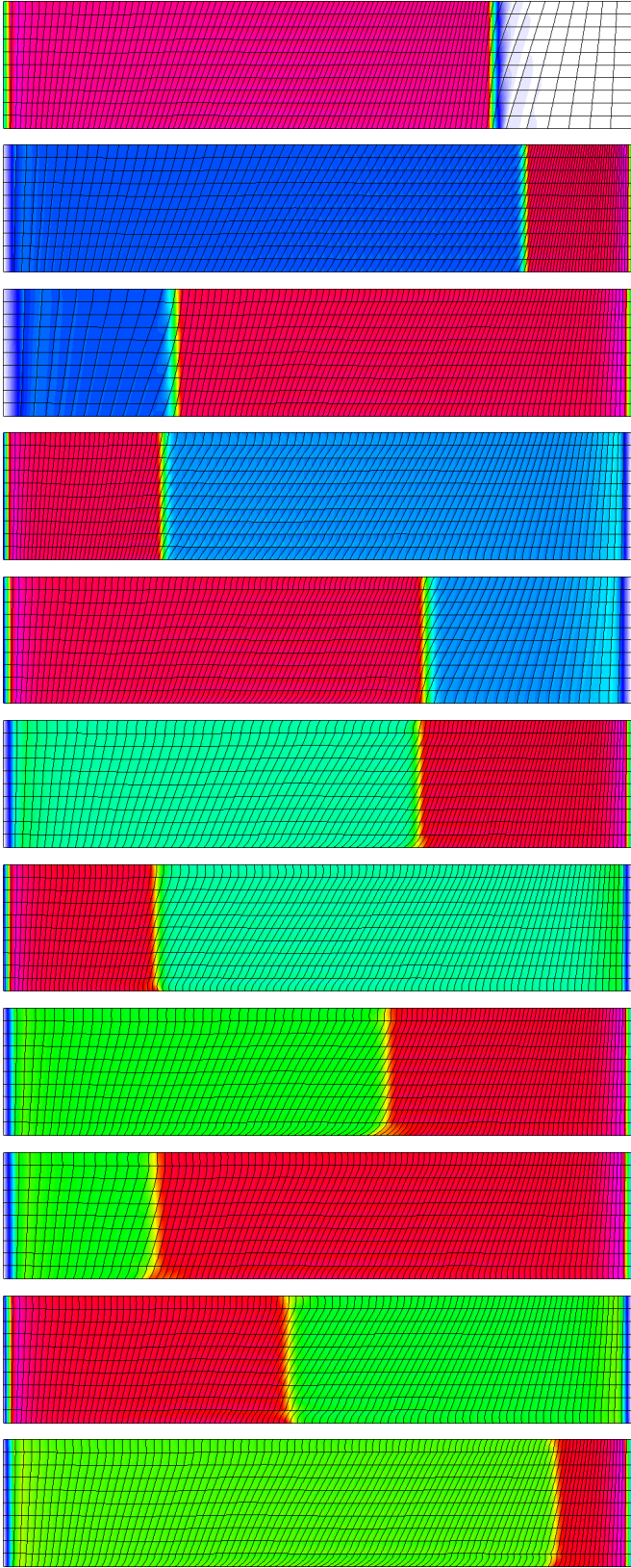
7

Figure 4: Curvilinear mesh and density field sampled at multiple points per zone for the cylindrical Saltzman piston problem at $t = 0.7, 0.8, 0.88, 0.92, 0.94, 0.96, 0.975, 0.985, 0.987, 0.99$ and 0.992 for a total of 7 bounces. Each image is rescaled to an aspect ratio of $5 : 1$.

wave, converting the initial internal energy into kinetic energy. The delta function energy source is approximated by setting the internal energy e to zero in all degrees of freedom except at the origin where the value is chosen so that the total internal energy is 1.

In Figure 5 we plot the density field and curvilinear mesh at the final time of $t = 1.0$. In Figure 6 we show scatter plots of the density versus the radius sampled at 9 points per zone and at 1 point per zone (at the zone center) on a sequence of refined meshes. The oscillations in the data near the shock front are at the sub-zonal level, the zone centered values do not exhibit this behavior. Note that in this calculation, the total numerical energy was conserved to machine precision for all time and we have convergence to the exact shock location, cf. Figure 1.
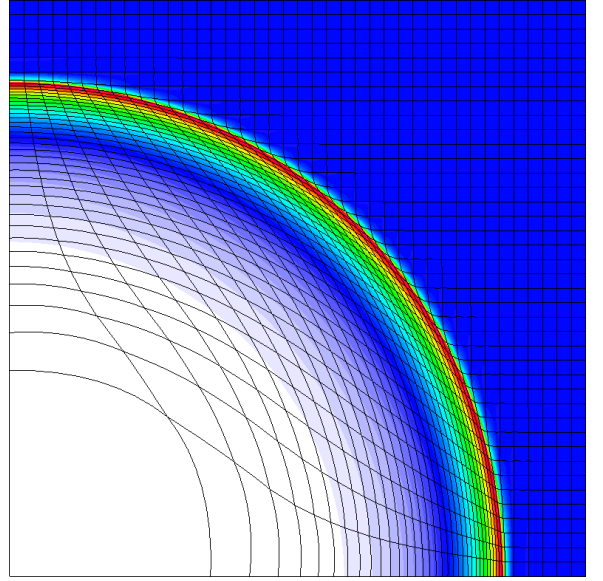
Figure 5: Curvilinear mesh and density field sampled at multiple points per zone for the axisymmetric Sedov problem on a 40×40 Cartesian grid at time $t = 1.0$.

4.3. Spherical Noh Implosion

The Noh problem consists of an ideal gas with $\gamma = 5/3$, initial density $\rho_0 = 1$ and initial energy $e_0 = 0$. The value of each velocity degree of freedom is initialized to a radial vector pointing toward the origin, $v = -\vec{r}/\|\vec{r}\|$. The initial velocity generates a spherical stagnation shock wave that propagates outward with a speed of $\frac{1}{3}$ and produces a peak post-shock density of $\rho = 64$.

In Figure 7 we plot the density field and curvilinear mesh at the final time of $t = 0.6$. In Figure 8 we show scatter plots of the density versus the radius sampled at 9 points per zone and at 1 point per zone (at the zone center) on a sequence of refined meshes. As with the previous problem, the oscillations in the data near the shock front are at the sub-zonal level, the zone centered values do not exhibit this behavior. Note that in this calculation, the total numerical energy was conserved to machine preserve for all time.

Density Scatter Plots: 9pt/zone
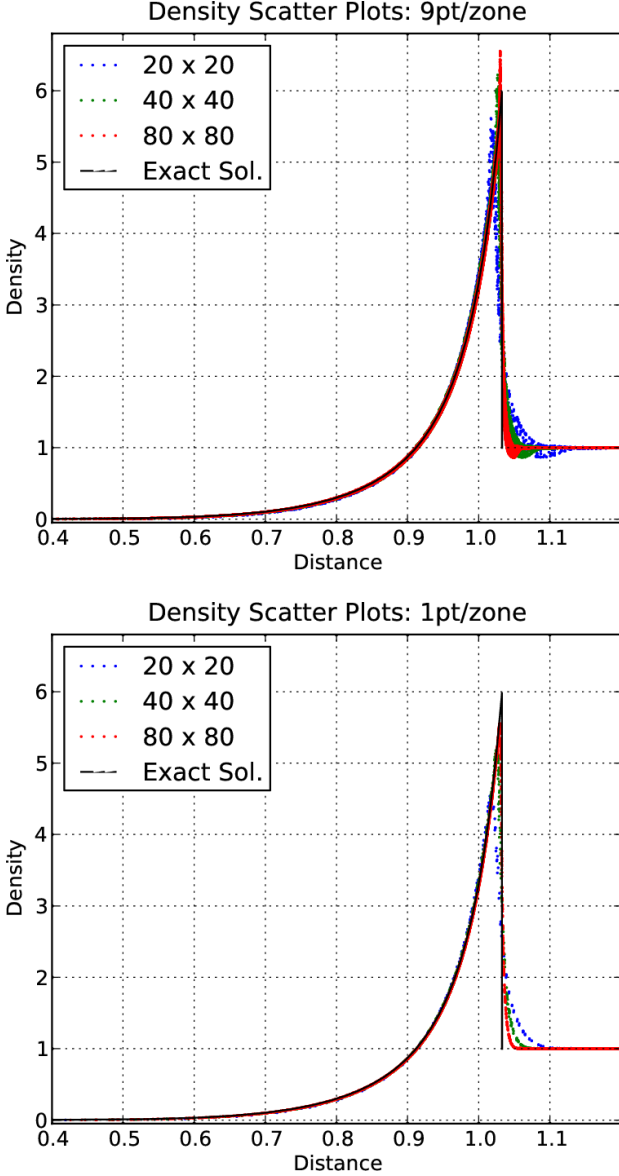
Density Scatter Plots: 1pt/zone

Figure 6: Scatter plots of density vs. radius sampled at 9 points per zone and 1 point per zone for the axisymmetric Sedov problem on a Cartesian grid.
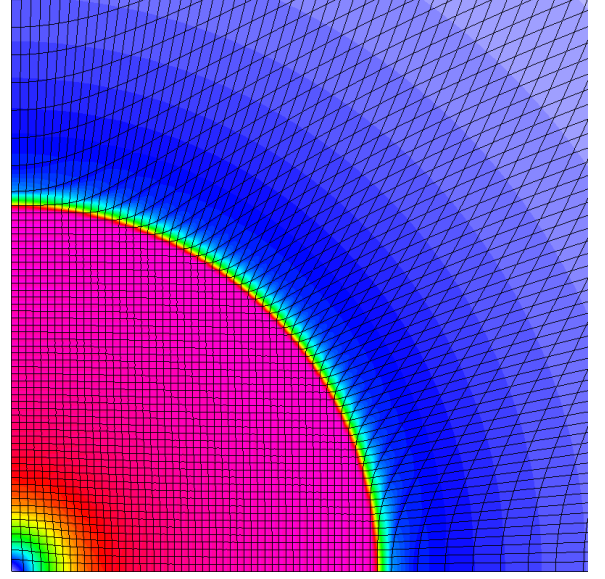

Figure 7: Curvilinear mesh and density field sampled at multiple points per zone for the axisymmetric Noh problem on a 64×64 Cartesian grid at time $t = 0.6$.

4.4. Axisymmetric Multi-Material Shock Triple Point Interaction

The triple point problem describes the interaction of three materials with ideal gas equations of state. The initial domain, materials and initial conditions are shown in Figure 9. Slip wall boundary conditions are imposed everywhere on the boundary, i.e. $v_z = 0$ at $z = 0$, $z = 7$ and $v_r = 0$ at $r = 0$, $r = 3$.

We discretize the problem using the Q_4-Q_3 finite element space pair (see [1]) which is based on bi-quartic continuous velocity and displacement spaces and bi-cubic discontinuous energy space. The initial mesh is a 56×24 uniform Cartesian mesh. For all discretization parameters we use their default values except for the tensor artificial viscosity where we use type 4 (see [1]) modified appropriately for the axisymmetric case.

In Figure 10, we present a sequence of snapshots of the computational mesh and density up to time $t = 5$. Note the extreme mesh distortion in the vortex region, near the horizontal material interface, as well as aroiund the $r = 0$ axis. Even in the presense of such extreme deformations our method still maintains its robustness.

In Figure 11, we plot the full 3D material domains at the final time $t = 5$ obtained by revolving the solution from the meridian cut about the axis of symmetry $r = 0$.

4.5. Multi-Material Spherical Implosion

Here we consider a simple 1D multi-material implosion problem on unstructured 2D meshes. The problem consists of a low density material with $\rho_1 = 0.05$ in the radial range $r \in [0, 1]$ surrounded by a shell of high density material $\rho_2 = 1.0$ in the radial range $r \in [1.0, 1.2]$. Each
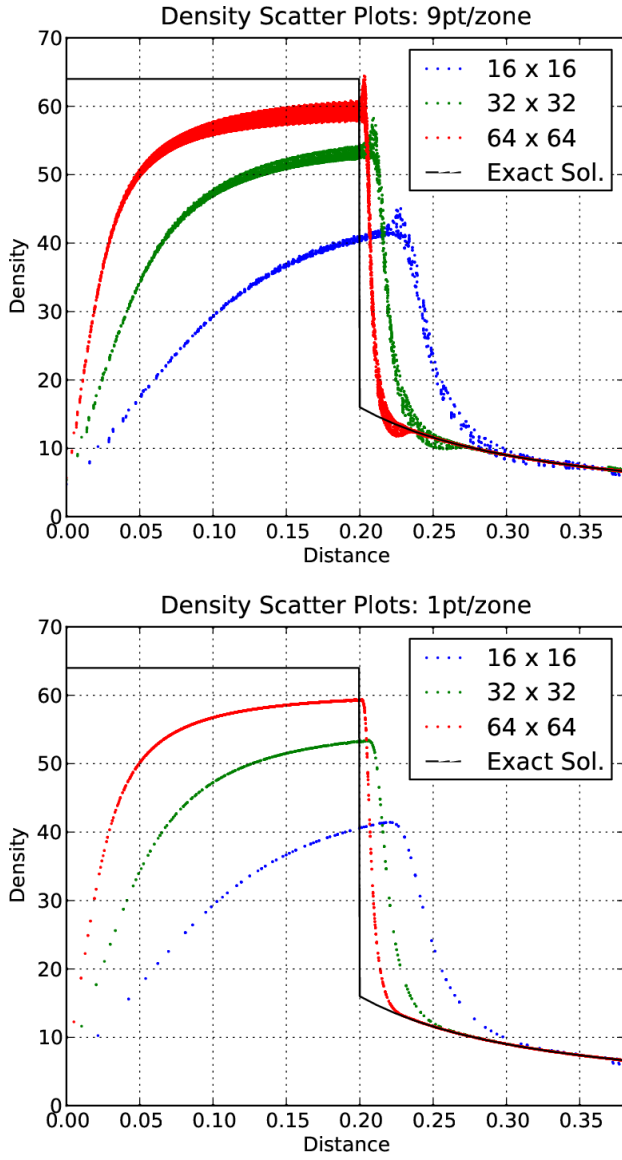
Figure 8: Scatter plots of density vs. radius sampled at 9 points per zone and 1 point per zone for the axisymmetric Noh problem on a Cartesian grid.
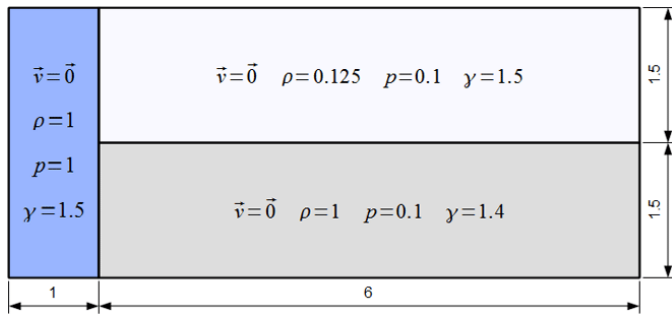

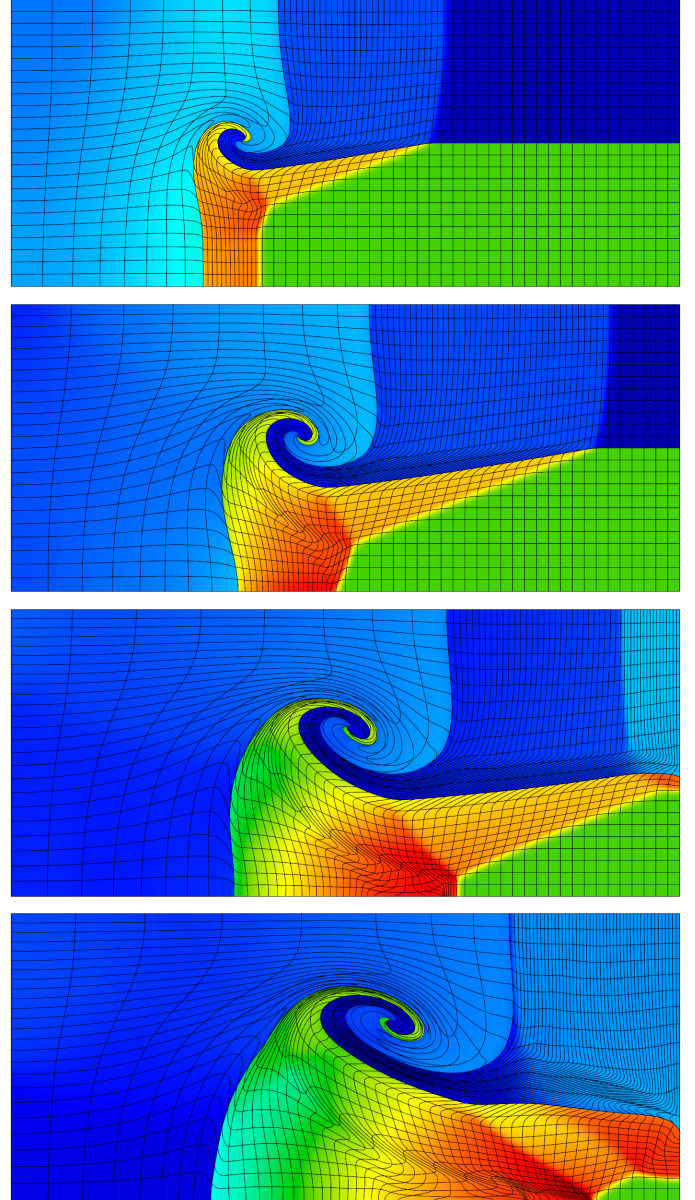Figure 9: Initial conditions for the axisymmetric multi-material shock triple point interaction problem.

Figure 10: Snapshots of density and curvilinear mesh for the axisymmetric triple point problem obtained using the Q_4-Q_3 method at $t = 2$, 3, 4, and 5 (top to bottom).
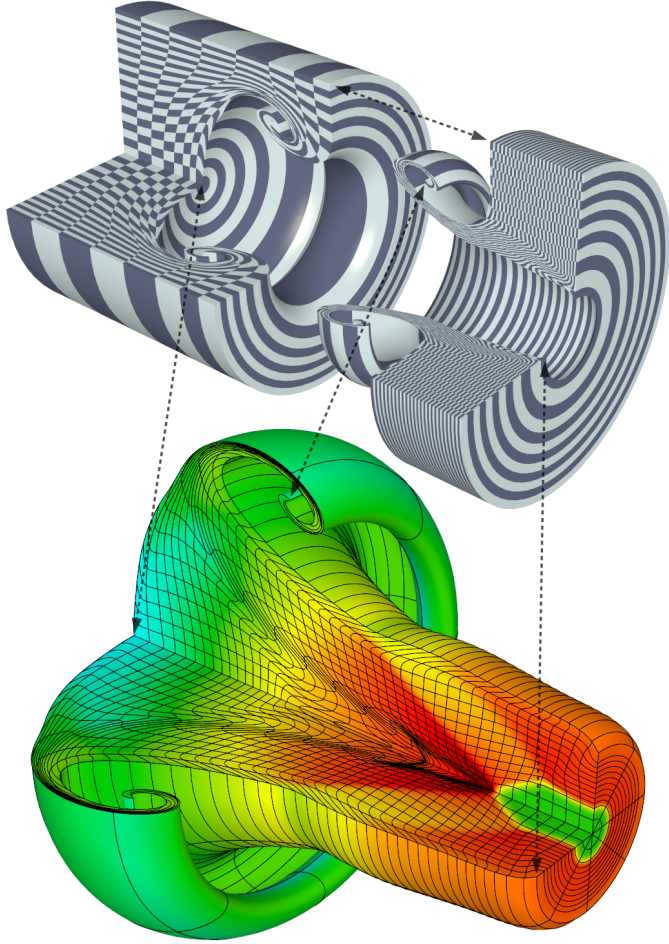
material is at an initial pressure of $p = 0.1$ and uses an ideal gas equation of state with $\gamma = 5/3$.

This problem was originally proposed by [23] for cylindrical symmetry. Here we make a simple modification for spherical symmetry, instead of applying a time dependent pressure source to the outermost radial surface of the problem, we apply a constant velocity source of $v = -5\vec{r}/\|\vec{r}\|$. The outer surface drives a spherical shock wave inward. Ideally, the interface between the high and low density materials should remain perfectly spherical for all time due to the spherical symmetry of the velocity drive. However, the discretization errors of the initial geometry of this surface and subsequent error introduced by the numerical algorithm will be amplified over time since the interface is subject to both Richtmyer-Meshkov (RM) and Rayleigh-Taylor (RT) instabilities.

In Figure 12 we show plots of the mesh and density on a log scale at three snapshots in time for the case of a uniform unstructured mesh. In Figure 13 we show identical plots for the same problem on a randomly perturbed unstructured mesh. In both cases, the initial mesh is curved by mapping all position degrees of freedom in the outer high density shell to a spherical surface. Note that the randomly perturbed mesh has both non-uniform angular spacing as well as non-uniform aspect ratios in the central "box" region. Maintaining spherical symmetry on such a mesh with a Lagrangian method is a non-trivial task, cf. Figure 2.

In Figure 14 we plot the average radius of the entire material interface using 5 points per edge for both cases and compare these to a reference 1D result (obtained from a high resolution 1D Lagrangian SGH calculation). Note that each mesh yields essentially identical results in the average radius and both are in good agreement with the 1D high resolution reference solution. In Figure 14 we also plot the normalized standard deviation of this radial surface which indicates the symmetry error over time. Note the degree to which the interface symmetry is preserved, even on the random mesh, with errors less that 0.1%.

5. Conclusions

In this paper we presented an extension of our high-order curvilinear finite element method for solving the equations of compressible hydrodynamics in a Lagrangian frame to the case of axisymmetric problems. This extension results in relatively simple modifications to the semi-discrete formulation, consisting of a rescaled momentum conservation equation and new radial terms in the pressure gradient and artificial viscosity forces, and was shown to exactly conserve total numerical energy. We also demonstrated via numerical examples the benefits of the new high order curvilinear axisymmetric discretization method, including: significant improvements in symmetry preservation for symmetric flows even when the underlying mesh is highly non-uniform; the ability to more accurately capture
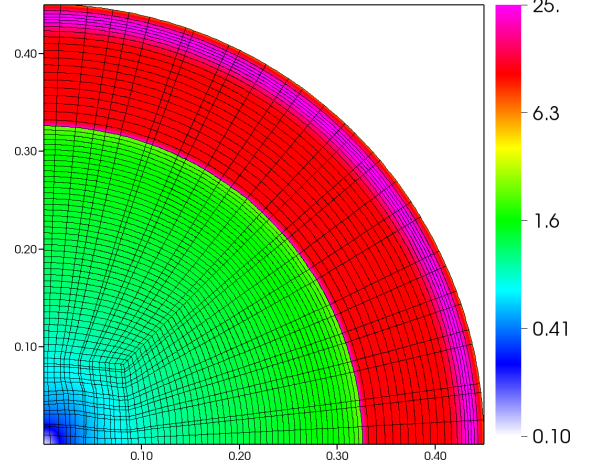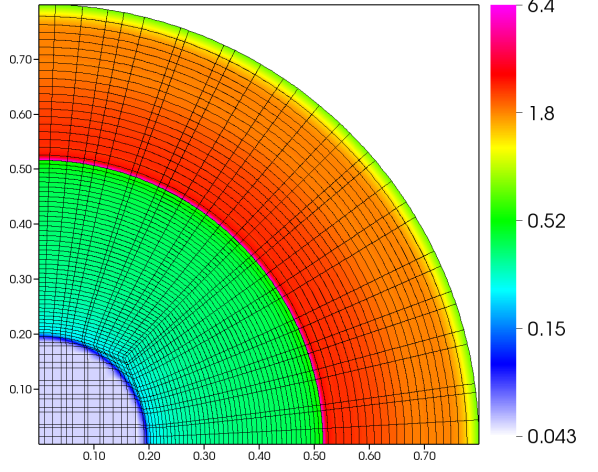

Figure 11: Full 3D visualization of the materials in the axisymmetric triple point problem obtained using the Q_4-Q_3 method at $t = 5$; revolved axisymmetric mesh (top) and density (bottom).
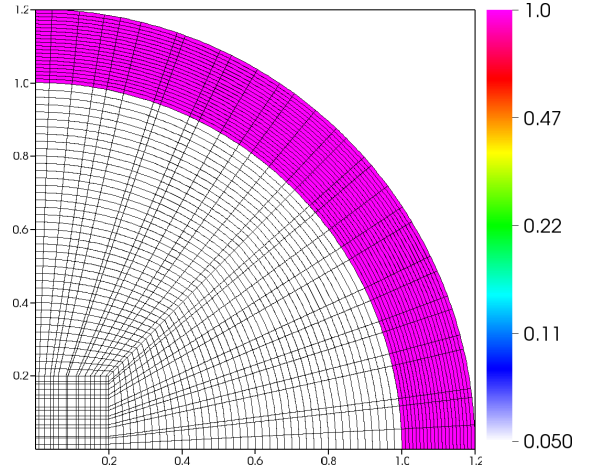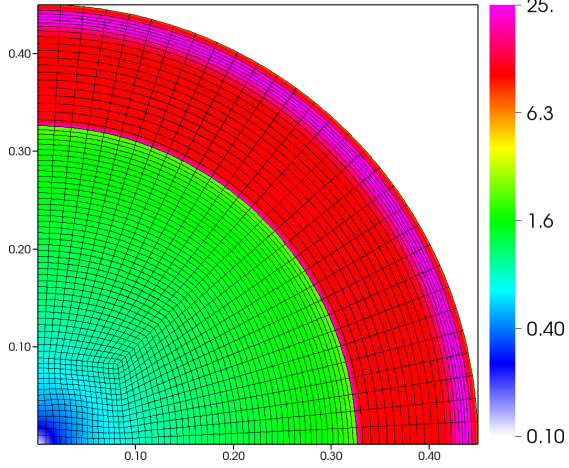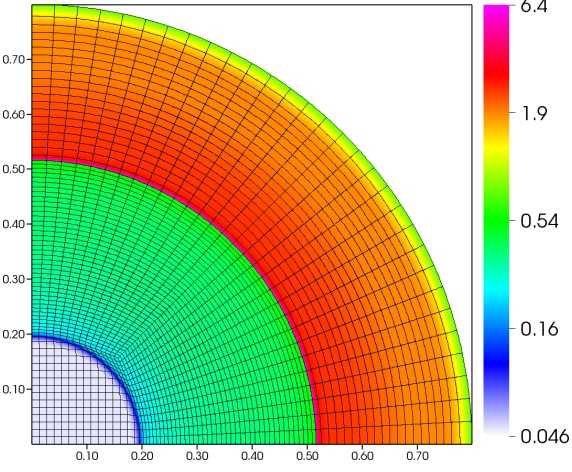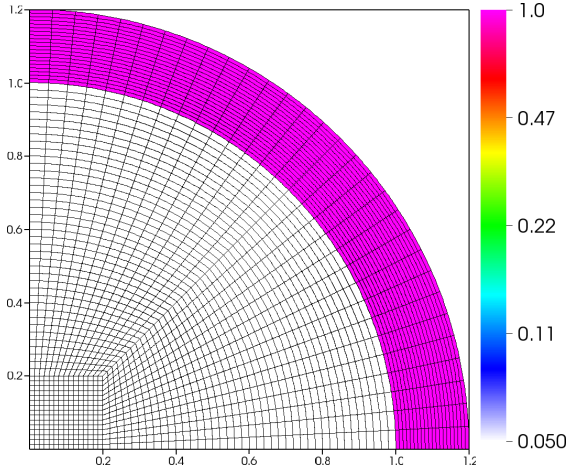
Figure 12: Snapshots of curvilinear mesh and density field (log scale) sampled at multiple points per zone at times $t = 0$, $t = 0.08$ and $t = 0.15$ for the axisymmetric multi-material spherical implosion problem on an unstructured uniform mesh.

Figure 13: Snapshots of curvilinear mesh and density field (log scale) sampled at multiple points per zone at times $t = 0$, $t = 0.08$ and $t = 0.15$ for the axisymmetric multi-material spherical implosion problem on an unstructured random mesh.

geometrical features of a flow region and maintain robustness with respect to mesh motion using curvilinear zones and high order bases; the elimination of the need for ad hoc hourglass filters; sharper resolution of a shock front for a given mesh resolution including the ability to represent a shock within a single zone; and a substantial reduction in mesh imprinting for shock wave propagation not aligned with the computational mesh.
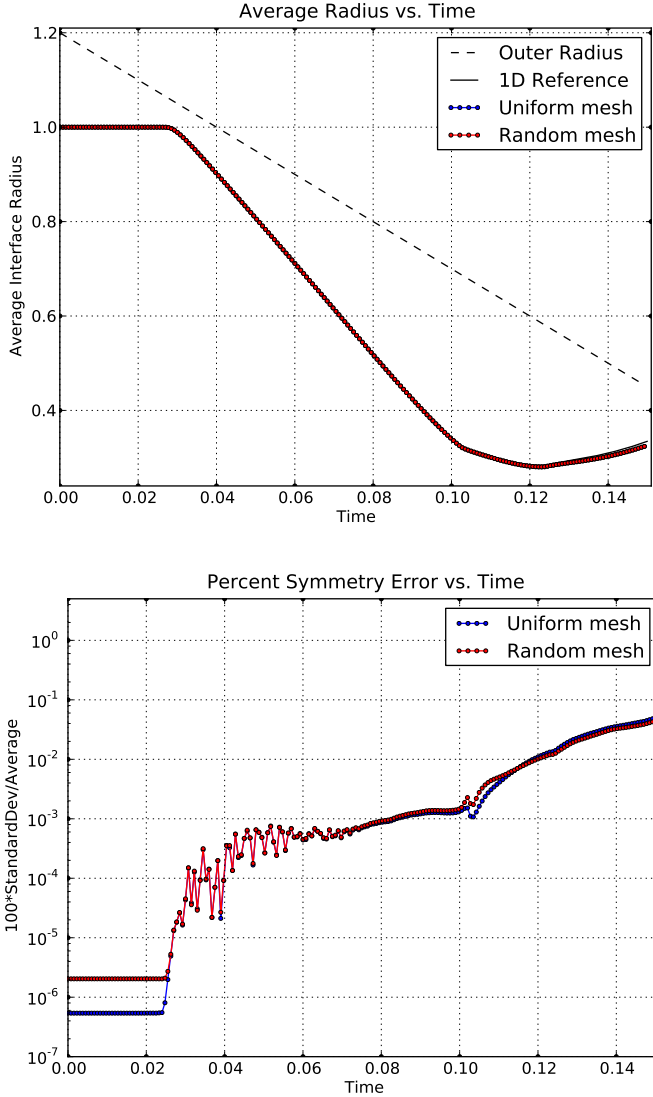

Figure 14: Average interface radius vs. time (*top*) and percent symmetry error vs. time (*bottom*) for the axisymmetric multi-material spherical implosion problem on an unstructured uniform and random mesh.

References

[1] V. A. Dobrev, Tz. V. Kolev, and R. N. Rieben. High order curvilinear finite element methods for Lagrangian hydrodynamics. *(submitted)*, 2011. Also available as LLNL technical report LLNL-JRNL-516394.

[2] H. Ockendon and J. Ockendon. *Waves and Compressible Flow*, volume 47 of *Texts in Applied Mathematics*. Springer-Verlag, 2004.

[3] D. J. Benson. Computational methods in Lagrangian and Eulerian hydrocodes. *Comput. Methods Appl. Mech. Engrg.*, 99:235–394, 1992.

[4] Ya. B. Zel'dovich and Yu. P. Raizer. *Physics of Shock Waves and High-Temperature Hydrodynamic Phenomena*. Academic Press, New York, 1967.

[5] J. Castor. *Radiation Hydrodynamics*. Cambridge University Press, Cambridge, UK, 2004.

[6] V. A. Dobrev, T. E. Ellis, Tz. V. Kolev, and R. N. Rieben. Curvilinear finite elements for Lagrangian hydrodyanmics. *Internat. J. Numer. Methods Fluids*, 65(11-12):1295–1310, 2010.

[7] M. L. Wilkins. *Methods in Computational Physics*, volume 3, chapter Calculation of Elastic-Plastic Flow. Academic Press, 1964.

[8] P. Whalen. Algebraic limitations on two dimensional hydrodynamics simulations. *J. Comput. Phys.*, 124(1):46–54, 1996.

[9] E. J. Caramana, D. E. Burton, M. J. Shashkov, and P. P. Whalen. The construction of compatible hydrodynamics algorithms utilizing conservation of total energy. *J. Comput. Phys.*, 146:227–262, 1998.

[10] L. Margolin and M. Shashkov. Using a curvilinear grid to construct symmetry-preserving discretizations for Lagrangian gas dynamics. *J. Comput. Phys.*, 149:389–417, 1999.

[11] K. Lipnikov and M. Shashkov. A framework for developing a mimetic tensor artificial viscosity for Lagrangian hydrocodes on arbitrary polygonal meshes. *J. Comput. Phys.*, 229(20):7911–7941, 2010.

[12] A. Barlow, D. Burton, and M. Shashkov. Compatible, energy and symmetry preserving 2d Lagrangian hydrodynamics in rz–cylindrical coordinates. *Proc. Comp. Sci. (ICCS)*, 1(1):1893–1901, 2010.

[13] P. Matejovic and V. Adamik. A one-point integration quadrilateral with hourglass control in axisymmetric geometry. *Comput. Methods Appl. Mech. Engrg.*, 70(3):301–320, 1988.

[14] P. Matejovic. Quadrilateral with high coarse-mesh accuracy for solid mechanics in axisymmetric geometry. *Comput. Methods Appl. Mech. Engrg.*, 88(2):241–258, 1991.

[15] P-H. Maire. A high-order cell-centered Lagrangian scheme for two-dimensional compressible fluid flows on unstructured meshes. *J. Comput. Phys.*, 228(7):2391–2425, 2009.

[16] L. I. Sedov. *Similarity and Dimensional Methods in Mechanics*. CRC Press, tenth edition, 1993.

[17] D. E. Burton. Multidimensional discretizations of conservation laws for unstructured polyhedral grids. Technical Report UCRL-JC-118306, Lawrence Livermore National Laboratory, 1994.

[18] E. J. Caramana and M. J. Shashkov. Elimination of artificial grid distortion and hourglass-type motions by means of Lagrangian subzonal masses and pressures. *J. Comput. Phys.*, 142(2):521–561, 1998.

[19] BLAST: High-order finite element Lagrangian hydrocode. http://www.llnl.gov/CASC/blast.

[20] MFEM: Modular parallel finite element methods library. http://mfem.googlecode.com.

[21] GLVis: OpenGL visualization tool. http://glvis.googlecode.com.

[22] J. K. Dukowicz and B. J. Meltz. Vorticity errors in multidimensional lagrangian codes. *J. Comput. Phys.*, 99(1):115–134, 1992.

[23] S. Galera, P-H. Maire, and J. Breil. A two-dimensional unstructured cell-centered multi-material ALE scheme using VOF interface reconstruction. *J. Comput. Phys.*, 229(16):5755–5787, 2010.